Lynx soft x-ray critical-angle transmission grating spectrometer

Hans Moritz Günther
Ralf K. Heilmann

SPIE.

Lynx soft x-ray critical-angle transmission grating spectrometer

Hans Moritz Günther[a,*] **and Ralf K. Heilmann**[a,b]
[a]Massachusetts Institute of Technology, MIT Kavli Institute for Astrophysics and Space Research, Cambridge, Massachusetts, United States
[b]Massachusetts Institute of Technology, Space Nanotechnology Laboratory, Cambridge, Massachusetts, United States

Abstract. Lynx is one of four Surveyor-class mission concept studies for the 2020 Astrophysics Decadal Survey. It features an x-ray telescope with an unprecedented collecting area of 2 m^2 at 1 keV and a point-spread function of 0.5 arc sec. We describe the status of critical-angle transmission (CAT) grating technology development and perform ray-traces for a CAT grating x-ray spectrometer that can reach high spectral resolving power $\lambda/\Delta\lambda > 5000$ (often exceeding 7500) and effective area around 4000 cm^2 in the soft x-ray band (0.2 to 2 keV). To achieve these characteristics, about two-thirds of the aperture must be covered with gratings. CAT gratings are mostly transparent at high energies, and thus hard x-rays can still be used for simultaneous imaging spectroscopy using a microcalorimeter array. We simulate several design scenarios and investigate how subaperturing can be most effectively used to increase performance. For large gratings, the resolving power is limited by the deviation of flat gratings from the ideal Rowland torus surface. Chirped gratings, i.e., gratings where the spacing of grating bars is variable, can overcome this limitation. Alignment tolerances in many degrees of freedom can be achieved with machining tolerances. We outline the development path to CAT grating performance improvements and discuss future ray-trace work to refine the design of the spectrometer. © *The Authors. Published by SPIE under a Creative Commons Attribution 4.0 Unported License. Distribution or reproduction of this work in whole or in part requires full attribution of the original publication, including its DOI.* [DOI: 10.1117/1.JATIS.5.2.021003]

Keywords: ray-tracing; x-ray optics; critical angle transmission grating; Lynx; Rowland torus.

Paper 18107SS received Nov. 5, 2018; accepted for publication Feb. 13, 2019; published online Mar. 8, 2019.

1 Introduction

In preparation for the 2020 Decadal Survey, NASA commissioned a study for a large x-ray mission. The concept for this mission is called Lynx, and it is envisioned to enable key science that cannot be done with other missions currently in operation or planned.[1,2] Compared to, e.g., Athena,[3,4] Lynx is an x-ray telescope that will have a narrow point-spread function (PSF) with a half-power-diameter (HPD) of only 0.5 arc sec, an effective area of 2 m^2 at 1 keV, and a 10 m focal length. A diffraction grating spectrometer is one of three notional science instruments. This special section of JATIS is dedicated to the Lynx development effort.

The Advanced Concepts Office (ACO) at NASA's Marshall Space Flight Center (MSFC) has performed instrument configuration studies for all instruments on the Lynx x-ray telescope, with the goal to produce realistic concepts for the technical implementation of the telescope and all of its instruments. These concepts can then become the basis for realistic mission resource (mass, power, etc.) and cost estimates.

The two instruments at the focus (the High Resolution X-ray Imager, HDXI, and the Lynx X-ray Microcalorimeter, LXM) sit on a lateral translation table that moves one instrument at a time into the focus. While microcalorimeters are superior to grating spectroscopy for high-energies, in soft x-rays (in the following, we will use this term to mean x-rays below 2 keV) dispersion gratings are unmatched in resolving power. This opens a range of new science questions that can be addressed with an x-ray grating spectrometer (XGS). Two prominent examples are

narrow and weak absorptions lines from intergalactic hot baryons expected in the halos of galaxies and galaxy clusters, and emission lines from stars from, e.g., coronal emission or the accretion shock of young stellar objects. In the later case, an accurate temperature diagnostic requires resolving hundreds of weak emission lines formed by different elements at different temperatures.

These science cases lead to the following requirements for the XGS:[5] Around the wavelength λ of the density and temperature sensitive O VII triplet (about 2.2 nm or 0.56 keV), the XGS shall deliver a resolving power $R = \lambda/\Delta\lambda > 5000$ and an effective area $A_{\text{eff}} > 4000$ cm^2. In this paper, we describe one possible design for the XGS that could deliver these requirements; to be conservative in these early stages, we plan to exceed both requirements by at least 10%. In this design, we make use of transmission gratings that are mounted blazed as "critical-angle transmission (CAT)" gratings.[6,7] CAT gratings have a significantly higher diffraction efficiency than the transmission gratings used on Chandra for most of the soft x-ray band, and the most efficient diffraction orders are at larger diffraction angles, leading to higher resolving power. As true transmission gratings, they have relaxed alignment tolerances and are lightweight. In addition, CAT gratings become essentially transparent at higher energies, keeping most of the flux available for simultaneous observations with the other instruments. The CATXGS is used as the XGS instrument in the Lynx Design Reference Mission. Alternatively, off-plane reflection gratings could be used and a design for those is discussed in Ref. 8 in this special section.

CAT gratings[6,7] are one of the enabling technologies for the Arcus XGS Explorer mission,[9] which underwent a NASA funded Phase A concept study in 2018. Arcus is designed for

*Address all correspondence to Hans Moritz Günther, E-mail: hgunther@mit.edu

$R > 2500$ with A_{eff} up to 350 cm^2 in the band between 1.2 and 5.0 nm wavelength.

In this paper, we expand on our previous work and describe the characteristics of CAT gratings and other parameters which provide input for our ray-trace simulations (Sec. 2). Detector technologies are covered in other articles in this special issue. CAT grating technology is described in Sec. 3. In Sec. 4, we explain the geometry of the spectrometer before we show the setup of our ray-trace simulations in Sec. 5. Ray-tracing results are shown in Sec. 6. We discuss several design options in Sec. 7 and future CAT grating development in Sec. 8 before we end with discussion and a summary (Sec. 9).

2 Boundary Conditions for the Spectrometer Design

The XGS consists of a fully retractable array of gratings mounted to the Lynx Mirror Assembly [LMA, consisting of the X-ray Mirror Assembly (XMA), pre- and postcollimators, contamination doors, and a structural cylinder] just downstream from the postcollimator, and a fixed array of pixelated readout sensors following the surface of the Rowland torus, mounted to the Integrated Science Instrument Module and offset by tens of cm from the telescope focus (Fig. 1).

The grating array extends from the innermost ($\sim$127 mm) to the outermost ($\sim$1.496 m) mirror radius. Due to the low mass of the gratings themselves, the support structures can be lightweight, too. The whole mass of the movable grating array is expected to be below 50 kg. The relaxed alignment tolerances (Sec. 6.3) in the transmission geometry also lead to more relaxed temperature control requirements. We expect that the CAT gratings will not require active temperature control beyond the thermal environment that is provided for the mirror array.

2.1 Lynx Mirrors

Three different main mirror technologies are under consideration for Lynx for a focal length of 10 m. Until a specific technology is chosen, we perform simulations without a detailed mirror model. Instead, we use an effective model, where we simulate a perfect mirror that focuses all rays from an on-axis source exactly to the focal point and then apply scattering to broaden the PSF to 0.5 arc sec HPD. This scatter can be applied in the plane of reflection or perpendicular to the plane of reflection (also called "out of plane"). If the mirror is made up of many different shells and each of those shells has a very sharp PSF, but they are misaligned with respect to each other (off-center error), we need to run simulations where in-plane and out-of-plane scatter contribute equally. If instead the mirror shells are well aligned, and the dominant broadening mechanism of the PSF is the figure error or scattering by particulates, the in-plane scatter should be larger than the out-of-plane scatter. In this case, subaperturing of the mirror assembly as discussed below can improve the spectral resolving power. To be conservative, we assume an equal contribution from in-plane and perpendicular scatter for most simulations.

The most important property of the mirror, however, is the effective area A_{eff} at different energies. Our simulations use tabulated values for effective area as a function of mirror radius and x-ray energy based on a silicon meta-shell mirror point design.[10] For a geometric ray-trace as we want to perform here, we have to assume some geometric configuration (size, position) of the mirror assembly. For most of our results, however, changing the A_{eff} of the mirror at some energy just acts as an overall scale factor for the A_{eff} of the XGS at that energy. There is some influence on resolving power R since the astigmatism depends on the physical dimensions, but this is not the dominating effect. Thus, to first order, changes in the mirror parameters will not lead to fundamental design changes of the XGS presented here.

2.2 Readout Sensors

At this early stage in the Lynx concept development, the decision was made to utilize the same Si-based readout technology and pixel format for the HDXI and the grating readout for the time being. The pixel size of 16×16 μm^2 is driven by the PSF oversampling requirement for the HDXI. In the case of the CATXGS, this leads to a vast oversampling of the 100 μm (FWHM) line spread function (LSF) required for $R = 5000$.
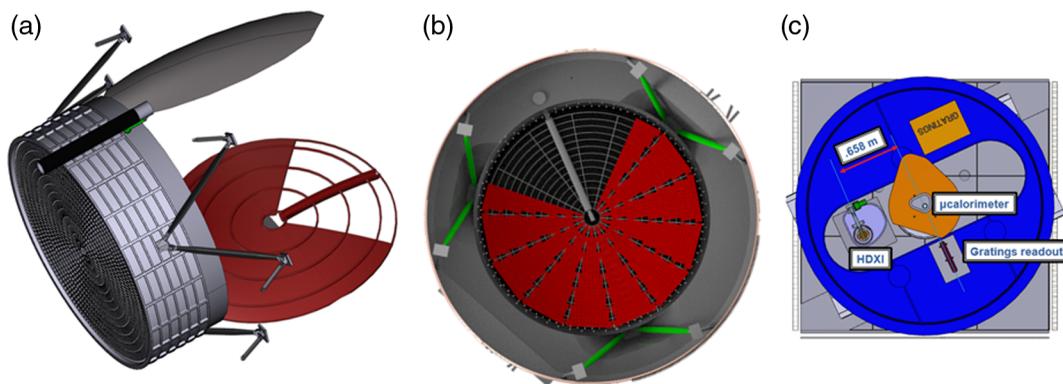

Fig. 1 CATXGS instrument views. (a) Contamination door (gray) and CAT grating array (red) retracted from the LMA. X rays enter the precollimator from the left. (b) Upstream view of the deployed CATXGS array. A configuration where the grating positions with the largest deviation from the Rowland torus are left uncovered (see discussion for Fig. 8) is shown. The array covers $\sim$264 deg in azimuth. The (green) bipod struts attach the mirror assembly to the optical bench assembly. (c) Downstream view of the Integrated Science Instrument Module with the movable focal plane instruments and the stationary linear CATXGS readout array. The configuration with the microcalorimeter instrument (dewar barely visible behind the filter assembly plate) in the focus position and the HDXI moved to the side is shown. Image credit: NASA MSFC/M. Baysinger.

Even for $R = 10,000$, such small pixels would oversample the LSF by more than a factor of three. If the HDXI sensor technology cannot provide curved sensors, then the image plane curvature limits the HDXI sensor size to ∼16 mm, and the CATXGS readout requires 18 sensors (including gaps). With curved sensors (possible with CCD technology, for example), the size could be increased to ∼64 mm, and only five sensors would be necessary. Moderate detector energy resolution (∼0.1 keV) is sufficient to assign detected events to a particular diffraction order. We assume a nominal silicon detector quantum efficiency as a function of energy, and in our model, the 18 sensors are separated by 0.5-mm wide gaps. The readout camera is designed with a two-degrees-of-freedom focus mechanism.

2.3 Filters

Most x-ray detectors are sensitive to optical and UV light and thus optical blocking filters need to be added to the design. For the simulations he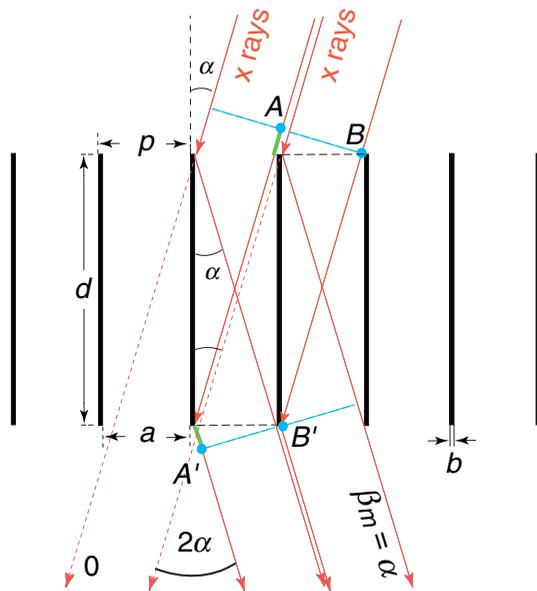re, we assume a 30-nm layer of Al topped with 10 nm of aluminum oxide, which may be directly deposited on the detectors, and 45 nm of Kapton mounted on a 95% transmissivity metal mesh.

3 CAT Grating Technology State-of-the-Art

The initial CAT grating design was conceived in 2005, and the technology has been under development since 2007.[11–18] CAT gratings feature freestanding ultrahigh aspect-ratio grating bars that are etched from the device layer of silicon-on-insulator (SOI) wafers.[6,7] The gratings are used with a blaze angle, meaning that the incoming photons are not parallel to the sides of the grating bars, but hit them at a grazing angle below the critical angle for total external reflection. This causes photons to be preferentially diffracted to one side of the incident beam. The peak of the distribution of diffracted photons is near the direction of specular reflection off the sidewalls, at about twice the blaze angle (see Fig. 2). The critical angle depends on the material of the grating and the photon energy. Here, we consider pure Si and Si that is coated with a ∼6-nm thick layer of platinum. The grating efficiency (the probability that a photon of a certain energy and angle is diffracted into a specific order) further depends on the geometric dimension of the grating bars. For the simulations here, we assume gratings that are 5.7 μm deep with a grating period of 200 nm and a 160-nm open gap between the bars. The grating bars are supported by integrated Si bars running perpendicular to them (L1 support structure, 5 μm period) and etched from the same layer. For high energies, the Si bars become highly transparent to x-ray photons and the structure acts as a weak phase-shifting grating which disperses a small fraction of photons into positive or negative orders.

The combined structure of grating bars and L1 support sits on top of 1-mm wide hexagons (L2 support structure) etched out of the SOI handle layer (see Fig. 3). We call the resulting structure a grating membrane. We assume that L1 and L2 structures cover about 10% of the geometric area each and reduce the photon throughput accordingly. We simulate different sizes for grating membranes surrounded by a mounting frame of 1 mm width. The absorption from the frames is included in our ray-tracing, but not the diffraction from L1 and L2 supports. Diffraction from L1 supports diverts a few percent of the photons without changing the spectral resolving power; most of these photons can be recovered. L2 diffraction is expected to be small, but may require small design changes in the L2 mesh. Both effects will be included in future work.
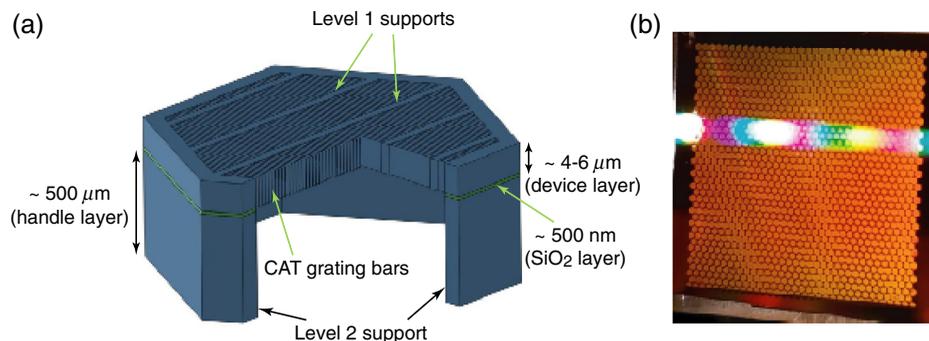

Fig. 2 Schematic cross section through a CAT grating of period p. The m'th diffraction order occurs at an angle β_m where the path length difference between AA' and BB' is $m\lambda$. The case where β_m coincides with the direction of specular reflection from the grating bar sidewalls ($|\beta_m| = |\alpha|$), i.e., blazing in the m'th order is shown.

Fig. 3 (a) Schematic depiction of the structural hierarchy of the CAT grating membrane (see text). (b) Photograph of a back-illuminated 32×32 mm² prototype CAT grating membrane, showing the hexagonal L2 mesh and optical diffraction from the L1 mesh.

Current state-of-the-art CAT gratings feature the same grating period and structural hierarchy, but slightly less challenging dimensions.

3.1 Current Grating Membrane Parameters, Diffraction Efficiency, and Resolving Power

We are currently producing 200-nm period CAT gratings with 4 μm depth, 140 nm gaps between bars, and size up to 32×32 mm^2 for the Arcus Explorer mission[9] (see Fig. 3). These gratings achieve >30% absolute diffraction efficiency at 2.38-nm wavelength (sum over blazed orders), including absorption by L1 and L2 supports.[19] The L2 mesh blocks ~19% of the area and the recently fabricated L1 meshes block between 10% and 18%. We have coated CAT gratings with a thin layer of Pt and demonstrated $R > 10,000$ in 18th order using Al-K radiation with a breadboard spectrometer setup.[20,21] Based on these results, CAT grating technology was vetted by the NASA Physics of the Cosmos (PCOS) Technology Review Board at Technology Readiness Level (TRL) 4 in 2016.

3.1.1 Alignment

Alignment of transmission gratings is relatively straightforward for a typical x-ray objective grating where the diffraction angles of interest are relatively small (<5 deg to 10 deg). We have measured the resolving power of CAT gratings in combination with azimuthally subapertured mirrors of 1 to 2 arc sec line-spread function (FWHM) made with different technologies: a single pair of slumped glass segments[20,21] and silicon-pore optic mirror modules.[19,22] In all cases, the measured resolving power met our requirements. For grating arrays, relative alignment between gratings is important. The tightest requirements are for grating roll (which sets the dispersion direction) and yaw (which sets the blaze angle and thus influences the diffraction efficiency and effective area). For Arcus, we developed a UV laser reflection tool that can be used for both roll and yaw alignment.[23] Roll alignment of up to four CAT gratings performed in air was successfully verified under simultaneous illumination with x rays from two coaligned silicon-pore optic mirror modules to within 5 arc min, meeting Arcus requirements.[19,22]

The specific alignment requirements for the CATXGS are derived from ray-trace results in Sec. 6.3.

3.1.2 Environmental testing

Environmental testing has been performed on two ~10×30 mm^2 prototype CAT gratings, each bonded to a titanium flexure frame. Both gratings were cycled six times under vacuum between −30°C and +35°C, with a ramp of 1°C/min and a dwell time of 15 min at each peak of the cycle. One grating was also vibration tested. Visible and SEM inspection showed no changes or damage to the gratings. Measurements of x-ray diffraction efficiency and resolving power before and after environmental testing did not produce any differences outside of measurement uncertainty between pre- and postenvironmental testing performance. More details are described in Ref. 22.

4 Layout of the Spectrometer

We design the spectrometer to follow the Rowland torus geometry.[24] All gratings are positioned on the surface of the Rowland torus where we chose the dimension of the torus such that the gratings are close to the mirrors because a longer distance improves the spectral resolving power (Figs. 4 and 5). The optical axis does not pass through the center of the Rowland circle, instead, the entire torus is tilted.[25,26] We orient the
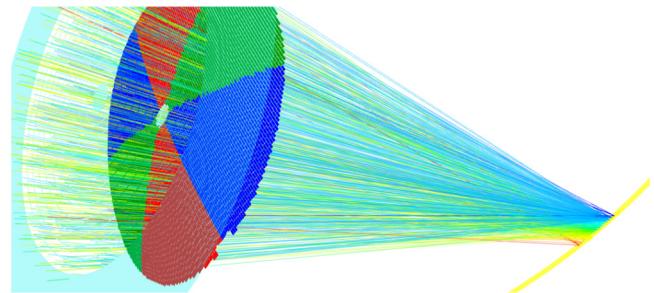
Fig. 5 Ray-trace simulation of Lynx XGS. The red, green, and blue rectangles are the active area of the CAT gratings. They are arranged on the surface of the Rowland torus. The yellow strip on the right marks the Rowland circle, where the detectors are located (detectors will only be placed on a very small fraction of the yellow strip shown here). Lines show the path of rays through the system. The simulation is monoenergetic. The different colors of the lines indicate into which diffraction order the photons are diffracted. Only photons that pass the gratings and hit the detector are shown, not those that are absorbed by, e.g., support structures.
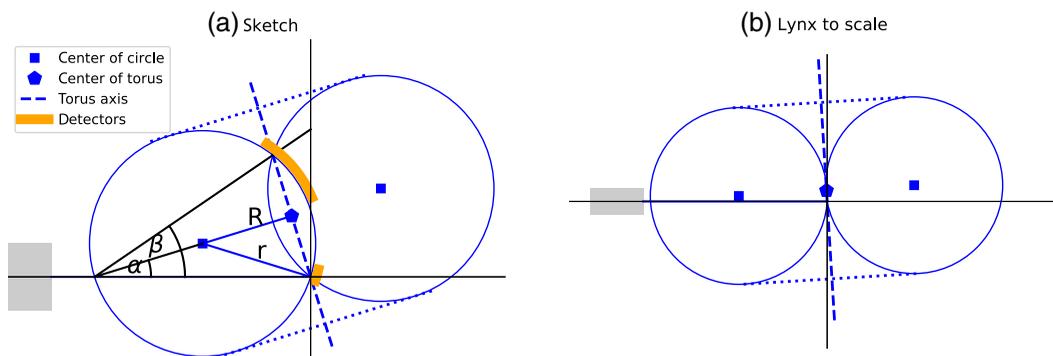

Fig. 4 (a) Conceptual sketch and (b) a to-scale drawing of the Lynx XGS configuration. The gray box on the left side of each panel marks the position of the mirror. The focal point is located at the origin of the coordinate system. The drawing shows a cut through the $z = 0$ plane, which also contains the symmetry axis of the torus. This gives two circles of radius r shown in blue. For the parameters chosen, those two circles overlap. The dotted lines are intended to help visualize the position of the torus. α is chosen close to the blaze angle to make the blazed grating facets close to tangential to the Rowland torus.

gratings such that a ray coming through the center of the grating has the prescribed blaze angle (1.6 deg in our design). Since the grating is flat and the torus is curved, most points on the grating do not match the Rowland torus exactly. Using a geometry with a tilted torus reduces the average difference.

The detectors are also placed on the Rowland torus. For CAT gratings, most of the diffracted power is found around twice the blaze angle. In addition, the zeroth-order must be covered by a detector since the distance between the zeroth-order and the diffracted signals is essential for wavelength calibration. Also, since the gratings mostly disperse soft x-rays, the zeroth-order contains most of the flux at higher energies and can be used for simultaneous imaging spectroscopy. In the case of Lynx, we plan to use the microcalorimeter as the primary zeroth-order detector for use with the grating spectrometer. Since the microcalorimeter is operated at very low temperatures, it must be mounted in a dewar with a radius around 300 mm. The XGS detectors must be placed at a larger distance from the focal point. We define x as the optical axis, y as the dispersion axis, and z is the cross-dispersion axis. We can then write the equation of a torus that is not tilted as

$$\begin{pmatrix} x \\ y \\ z \end{pmatrix} = \begin{pmatrix} (R + r \cos \theta) \cos \varphi \\ r \sin \theta \\ (R + r \cos \theta) \sin \varphi \end{pmatrix}. \qquad (1)$$

When we talk about the "Rowland circle," we mean the points that fulfill Eq. (1) with $\varphi = 0$, which gives us a circle in the (x, y) plane. Equation (1) can be generalized to tori where the center $\vec{c}$ does not coincide with the origin of the coordinate system and the axis of symmetry is not parallel to one of the axes of the coordinate system. The axis of symmetry is given by a unit vector $\vec{e}_y$. We define a vector $\vec{e}_R(\varphi) = \vec{e}_x \cos \varphi + \vec{e}_z \sin \varphi$ and can now write a generalized torus equation for points $\vec{p}$:

$$\vec{p}(\varphi, \theta) = \vec{c} + R\vec{e}_R(\varphi) + r[\vec{e}_y \sin \theta + \vec{e}_R(\varphi) \cos \theta]. \qquad (2)$$

For a torus that is translated and rotated with respect to the coordinate system, we only need to rotate the $\vec{e}_x$, $\vec{e}_y$, and $\vec{e}_z$ and specify $\vec{c}$. For different blaze angles, we need to tilt the torus differently, leading to different $\vec{e}_x$, $\vec{e}_y$, and $\vec{e}_z$ and different $\vec{c}$. For this spectrometer, we chose $r = 4810$ mm and $R = 4773$ mm. The vectors defined above are $\vec{c} = (36.2, 588.3, 0)$ in mm, $\vec{e}_x = (0.998, -0.061, 0)$, $\vec{e}_y = (0.061, 0.0998, 0)$, and $\vec{e}_z = (0, 0, 1)$. The telescope focus is at $(0, 0, 0)$. Figure 4 shows the geometry and Fig. 5 shows a rendering of a ray-trace in three-dimension (3-D), where CAT gratings are shown as small colored rectangles. The radii of the inner and outer shells of the mirror limit the area that can be covered with CAT gratings. In the following, we investigate scenarios with gratings of different size and different arraying strategies, where some of the area covered in Fig. 5 may be left free to optimize the spectral resolving power of the instrument.

5 Setup of the Ray-Trace

We use the MARXS code for our ray-trace.[27,28] MARXS is a Python-based Monte-Carlo ray-trace code that is available in a Github repository under an open-source license at: https://github.com/chandra-marx/marxs. Code specifically for the Lynx XGS can be found at https://github.com/hamogu/marxs-lynx/. The MARXS code is tested with hundreds of unit tests and also verified by comparison to laboratory data and Chandra

observations. MARXS performs a geometric ray-trace. For details of the implementation, we refer to the links and references, but due to the importance for this study, we detail the 3-D grating equation used. In a very general from, the grating equation can be written as

$$\vec{p}' \times \vec{n} = \vec{p} \times \vec{n} + (m\lambda/d)\vec{l}, \qquad (3)$$

for a ray with wavelength λ and direction $\vec{p}$ incident upon a diffraction grating of period d with a normal to the surface of the grating membrane $\vec{n}$. The grating lines are assumed to be parallel to the direction $\vec{l}$. $\vec{d}$ is a second vector in the plane of the grating membrane with $\vec{d} = \vec{n} \times \vec{l}$. Taking the dot product of Eq. (3) with $\vec{d}$ and $\vec{l}$, respectively, it can be shown that a ray diffracting into order m will propagate in a direction $\vec{p}'$ determined by the conditions:

$$\vec{p}' \cdot \vec{l} = \vec{p} \cdot \vec{l} \quad \vec{p}' \cdot \vec{d} = \vec{p} \cdot \vec{d} + \frac{m\lambda}{d}.$$

Optical properties as discussed in Sec. 2 are read in from data tables. Diffraction effects from the finite aperture of the individual mirror shells are not considered here but will become relevant for the innermost mirror shells at the lowest energies of interest. For example, at 0.2 keV, we estimate the diffraction limit alone—averaged over the whole mirror aperture—to be on the order of 0.3 to 0.4 arc sec (HPD).[29,30]

We set up four different configurations for the XGS, with different mirror properties, grating sizes, and grating properties. These scenarios are chosen to explore the parameter space of possible XGS configurations; they are not carefully optimized to obtain maximum performance. On the one hand, using larger gratings reduces the number of gratings required and thus the area lost to grating frames and mounting structures. A design with fewer gratings also reduces cost and production time, but there are practical limits to the grating size that can be fabricated. On the other hand, smaller gratings can be arranged to follow the surface of the Rowland torus better, while larger flat gratings will on average deviate more from the torus surface. This increases optical aberrations and limits the spectral resolving power. We simulate the following configurations:

- 50 mm × 20 mm gratings: This requires almost 5500 gratings to fill the aperture, but all gratings are identical. The grating bars run parallel to the long side of the grating, i.e., the short side is mounted parallel to the dispersion direction. As shown below, in this configuration, the spectral resolving power is sufficient everywhere. This is our baseline scenario; unless explicitly stated, the figures and the discussion below refer to simulations in this setup.

- 50 mm × 50 mm gratings: This requires less than half the gratings (about 2500) to fill the aperture, but the larger size means that in some locations of the aperture the deviation from the Rowland circle is too large to meet the resolving power requirements.

- 80 mm × 160 mm gratings with a chirp, i.e., with grating period that varies along the grating. The chirp can compensate for most of the loss in resolving power due to the deviation from the Rowland torus surface, so larger gratings can be used. At this size, only about 500 gratings
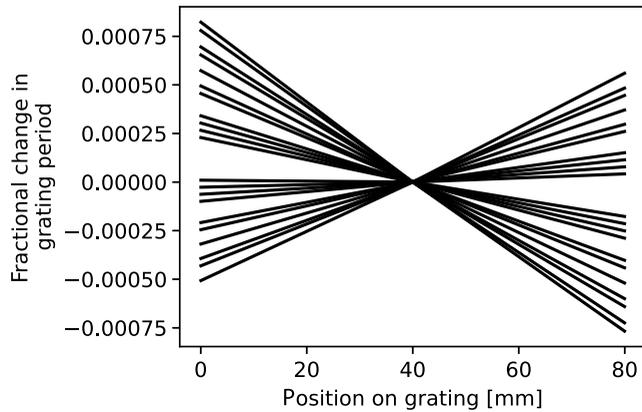
Fig. 6 Chirped gratings have a grating period that is not constant, but changes with position on the grating. The plot shows the required fractional change in grating period for a representative subset of all gratings in the "chirped" scenario.

Fig. 7 Histogram of diffracted photon positions on the Rowland circle for a simulation with a continuum source. The zeroth-order is located at 0 mm.

would be required, but the chirp is different for different gratings (Fig. 6). (In practice, the chirp prescriptions for gratings close to each other are very similar and it is probably sufficient to manufacture just a few different types.) The size of 80 mm × 160 mm is near the upper limit for a grating that could be etched from a 200-mm wafer. Smaller gratings with a chirp could be used, too, e.g., for 80 mm × 80 mm the resolving power will be just slightly better, but the effective area will be reduced by a very small amount due to the extra frame area.

- 50 mm × 20 mm grating as in the first case, but here we assume that the Lynx mirror PSF is not dominated by off-center errors, but by figure errors and scattering. The parameters are chosen to give the same overall PSF width, but subaperturing can be used to increase the spectral resolving power.

For the scenario with chirped gratings, we numerically determine the variations in grating period across a grating as follows: we ray-trace a ray pointing toward the focal point through the center of the grating, and two more rays intersecting the edges of the gratings. For those outer two rays, we numerically optimize the grating constant, until they hit the same detector location where the central ray is detected. That gives us three points with the required grating constant for each grating. We then simply perform a spline interpolation between these three points, but it turns out that these do not significantly deviate from a linear dependence (see Fig. 6). We use rays at 0.6 keV with a diffraction order selected to match the blaze peak for the optimization; since the required chirp depends on energy and diffraction order, the resolving power will decrease slightly for other energies and off-blaze diffraction orders.

6 Ray-Tracing Results

In this section, we present results from our ray-trace studies. We first confirm the detector position and then take a close look at the different scenarios at an exemplary energy (0.6 keV) chosen in the waveband of interest before we derive alignment tolerances and the resolving power and effective area for our canonical scenario.
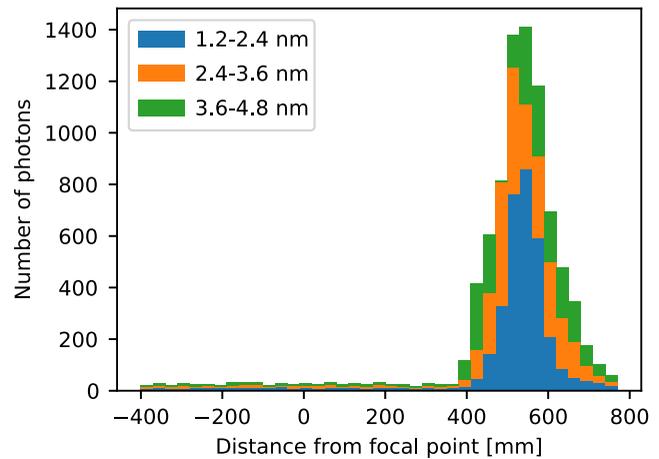
6.1 Position of Detector

Figure 7 shows a histogram of the position of diffracted photons for a simulation with a flat input spectrum. The blaze peak where most photons end up is clearly visible. The position and the width of this blaze peak can be derived directly from the input data on the grating efficiencies, but it is useful to check this with a ray-trace to see how nonideal effects broaden the peak. Because the grating facets are flat, but the photon beam is converging, the nominal blaze angle is only realized in the center of the grating, while all other rays have slightly different blaze angles. The figure shows that the photon distribution peaks about 550 mm from the zeroth-order and a detector array that extends from $y \sim 400$ to 700 mm as currently baselined catches the majority of the photons. However, a slightly larger number of photons would be detected for a longer detector array. This becomes more important for gratings of larger size, because the range of blaze angles is larger in that scenario.

6.2 Line Spread Function

We define the resolving power as: $R = \frac{\lambda}{\Delta\lambda} = \frac{d_x}{\text{FWHM}}$, where λ is the wavelength of a spectral line with negligible intrinsic width, and $\Delta\lambda$ is the observed width of this feature. Since the detector does not give the wavelength directly, d_x and the FWHM are linear distances measured as follows: events that hit a detector are projected (not propagated, that would bring them out of focus) into a plane. The FWMH is the full-width at half-maximum of the event distribution and d_x is the distance between the center of a diffracted order and the center of the zeroth-order.

Figure 8 shows the distribution of 0.6 keV photons diffracted into the sixth-order on the detector for our scenarios. The left plot in the figure shows the position of the gratings in the mirror aperture plane. Gratings are colored according to the azimuthal angle from the dispersion direction. In the other panels, photons are colored according to the grating they passed through.

Figure 9 displays the same data in a different way: photons are binned according to the position of the grating they passed through, and that distribution is shown along the dispersion axis, called the LSF. The resolving power R is given by the width of the photons' distribution in Fig. 9; narrower peaks mean a better R. For all the scenarios, the photons passing through gratings
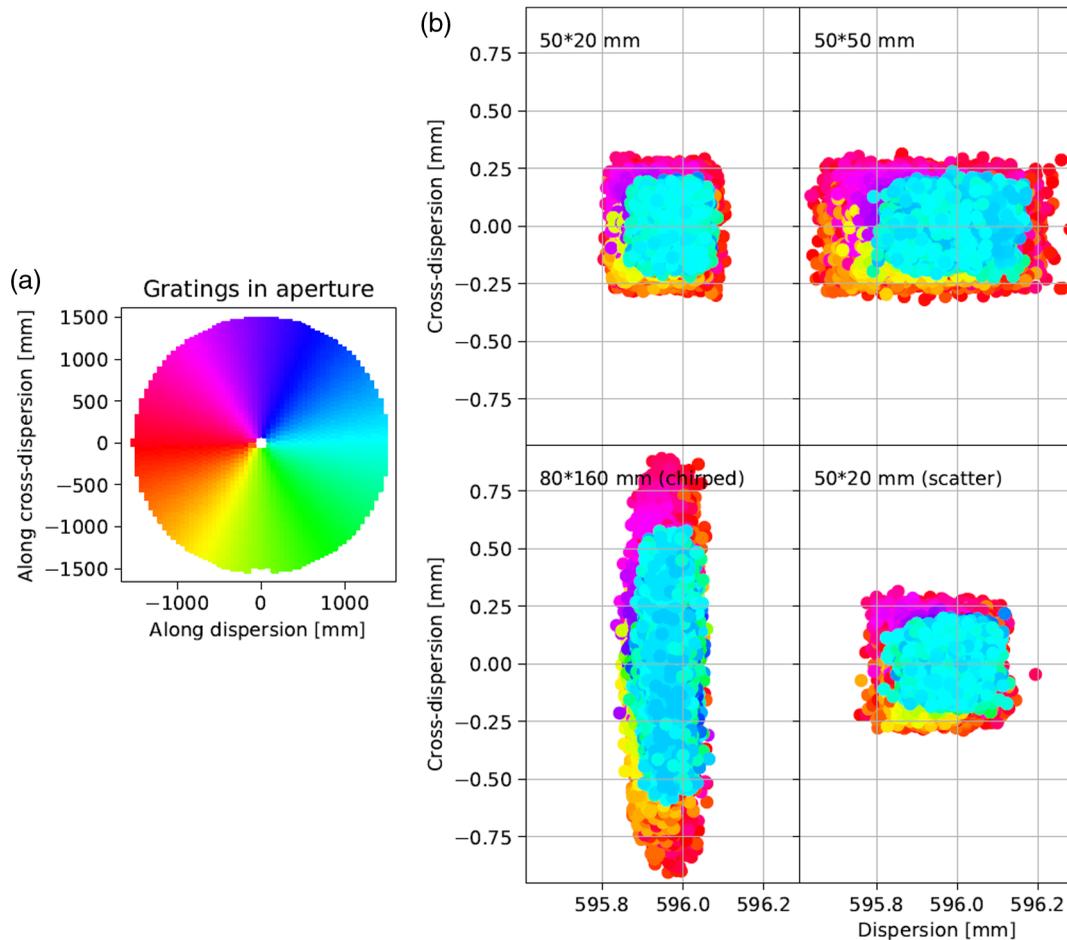
Fig. 8 (a) Position of gratings in the aperture plane. The placement of gratings is so dense that they appear continuous in this plot, but in reality there is space for a 1-mm wide frame around each grating. The gratings are color coded by angle relative to the dispersion direction (positive y-axis, here oriented in the horizontal direction). (b) Distribution of photons in the sixth-order for different CAT grating sizes and mirror scattering properties for photons of 0.6 keV. Each dot represents a single detected photon, color coded by the grating it passed.

located close to perpendicular to the dispersion direction (green line in Fig. 9) have the sharpest peaks. The other lines differ from the green line in two ways: they are often wider and in some cases their peaks are shifted. The width of the distribution is due to the intrinsic mirror PSF (which is the same in these simulations over the entire aperture) and the fact that the gratings deviate from the Rowland torus. In our simulations, the gratings are placed such that the center of each grating matches the Rowland torus. Because of the tilt of the torus, gratings located in the range 60 deg to 90 deg are almost tangential to the torus surface and have the smallest average deviation and thus the sharpest LSF. Larger gratings have larger average deviations than smaller gratings and thus the green LSF in the 50 mm × 20 mm scenarios is narrower than in the 50 mm × 50 mm scenario. Gratings located at larger or smaller angles cannot be tangential because they have to be rotated to match the blaze angle specification. Thus, they deviate more from the surface of the torus, leading to wider LSFs (lower R). Thus, these simulations show that a higher R can be achieved if only certain parts of the aperture are filled with gratings.

A second effect is the shift in the peak of the LSF between the green line and the other angles' ranges in Fig. 9. This is due to our naive way of placing the gratings. Photons that pass the

grating "outside" the Rowland torus travel further after they are diffracted and thus are detected at larger dispersion coordinates. Conversely, photons intersecting the grating "inside" the Rowland torus are detected at a smaller dispersion coordinate. At some locations, the gratings are mostly tangential to the Rowland torus, which means that almost the entire grating surface sits "outside" and thus photons are systematically send to larger dispersion coordinates; in other locations, half of the grating sits "inside." These shifts can be corrected by optimizing the grating position to reduce the average deviation from the Rowland torus and we will study this effect in more detail in future work. In our current simulations, this is not done and thus the R we derive is a lower bound to the value one would see with optimized grating placement. For example, for a simulation that covers the range in angles, e.g., 30 deg to 120 deg in the 50 mm × 50 mm scenario, we would see the combined LSF from adding the orange, green, and red curves, which is wider than it would be for an optimized grating placement that effectively shifts all three curves to have the same peak before adding them up.

We now compare the different scenarios in Fig. 9 to our baseline of 50 mm × 20 mm gratings. Simply using larger gratings reduces R as can be seen from comparing 50 mm × 20 mm to
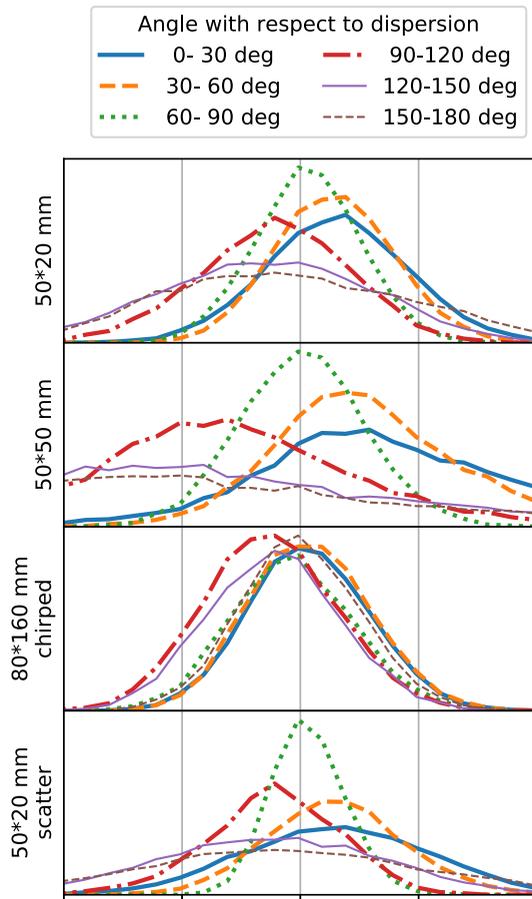
Fig. 9 Distribution of detected photons in the dispersion direction for different subaperture angles. The scaling along the y direction is arbitrary in this figure. The zero point of the x-axis is set to be the center of the simulated distribution.

Fig. 10 Trade-off between R and A_{eff} for different grating sizes and mirror scenarios for observations at 0.6 keV.

the 50 mm × 50 mm. However, with a relatively simple chirp applied, even much larger gratings such as 80 mm × 160 mm can recover the best R seen in the baseline case. With a chirp, essentially the same R is observed for any grating position. If the entire aperture does not have to be filled with gratings, the grating locations can be chosen based on engineering constraints without compromising R.

The two scenarios 50 mm × 20 mm and 50 mm × 20 mm (scatter) use the same grating locations, but differ in the scatter properties of the mirror. If the mirror PSF is dominated by figure errors and scattering, then subaperturing will increase R a lot more than in the conservative baseline 50 mm × 20 mm scenario where the PSF is dominated by off-center errors.

Thus, in all scenarios except for chirped gratings, there is a trade-off where subaperturing can increase R at the cost of reducing the effective area of the spectrometer. For each subaperture angle, we calculate R and A_{eff} (Fig. 10). A higher R goes along with using fewer gratings and thus a lower A_{eff}. 50 mm × 20 mm gratings can deliver $R > 5000$ for both mirror scenarios we simulate here, while 50 mm × 50 mm gratings deliver R below the requirements for all subaperturing angles that provide $A_{eff} > 4000$ cm^2.

At this early stage of development, we need to plan for a resolving power that is above the minimum requirement, since in practice, the number for R will degrade due to misalignments during grating mounting and the assembly of the XGS. If larger
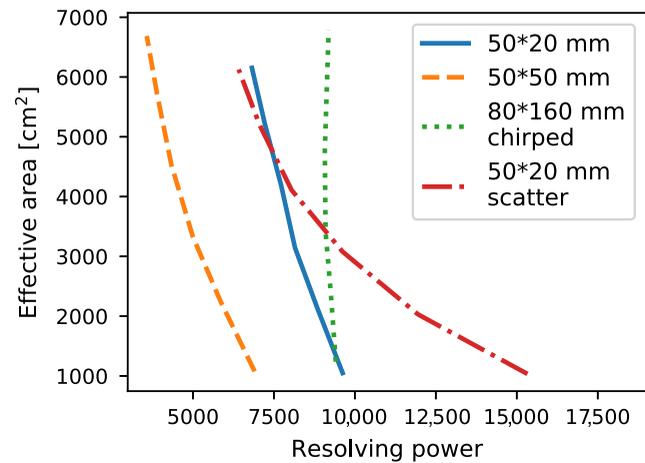
misalignments are tolerable, the assembly will be quicker, faster, and cheaper since fewer and less elaborate alignment steps are required.

On the other hand, the simulations shown in Fig. 10 assume a very simple subaperturing strategy, where the wedge filled with gratings is symmetric to the z axis (the cross-dispersion direction). Since the broadening of the line is not symmetric between the positive and negative x-axis (Fig. 8), a better subaperturing strategy would be to add more gratings to the right than to the left, which will improve R.

6.3 Alignment Requirements

Ray-tracing is a good tool to evaluate alignment requirements. We present simulations for our baseline 50 mm × 20 mm scenario filling the whole aperture with gratings.

In the simulations, all alignment is done with respect to the coordinate system established by the mirror (thus, by definition, the mirror is always aligned with the coordinate system). We treat all degrees of freedom independently, i.e., we change the alignment in just one degree of freedom at a time. This is simply a computational limitation. In order to simulate 20 steps in each rotation or translation axis (six degrees of freedom) for the grating assembly, each grating with respect to the global grating assembly, the detector assembly, and individual elements in the detector with respect to the detector assembly would require 20^{4*6} simulations.

Figure 11 shows examples of such calculations for rotation of the CAT grating assembly around the hinge located on one side of the grating assembly (Fig. 1); rotation around other points might yield different results. Also, these simulations are done assuming that the entire aperture is filled with gratings. The gratings located furthest from the hinge move the largest distance for any rotation. If those parts of the aperture are left free, the requirements on the alignment will be looser. x is the optical axis, y is the dispersion axis, and z is the cross-dispersion axis. Figure 11 shows that R is sensitive to rotations around all three axes. Rotation around y or z will bring some gratings "above" and others "below" the surface of the Rowland torus. This significantly broadens the LSF, reducing R by 10% for a rotation of 3 arc min. Rotation around z (the cross-dispersion direction) also changes the blaze angle and thus A_{eff} declines. Rotation around x has no effect on A_{eff} until the angle becomes so large
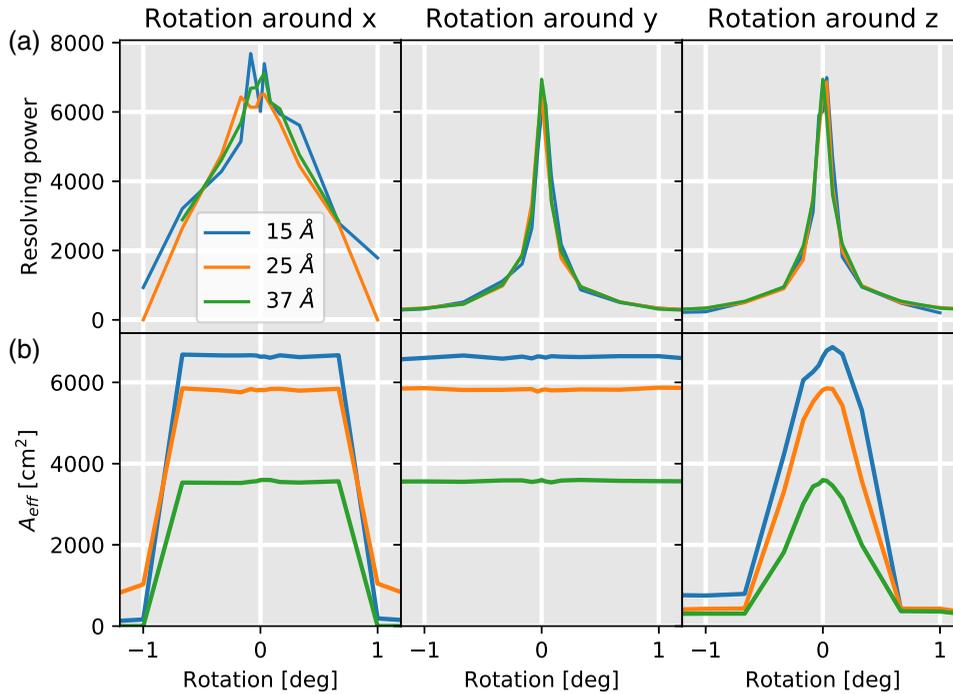
Fig. 11 Change in (a) resolving power and (b) effective area if the entire mechanical structure that holds all gratings is rotated.

that the order drops off the detectors. However, a rotation around the hinge moves gratings off their position on the Rowland torus and thus R becomes lower. We also performed simulations assuming the center of rotation is on the optical axis. In this case, R is much less sensitive to rotations around x.

The example shown in Fig. 11 is particularly relevant for the XGS because it sets not only the alignment during the assembly but also the requirements on the accuracy of swinging the grating structure into and out of the beam between observations. Note that requirements on the repeatability for swinging the gratings in and out are slightly different. A shift in x or a rotation around z will shift the mean of the photon distribution along the dispersion direction of the read-out. This has little effect on R and the position can be calibrated in flight easily, thus the requirements discussed above are loose, but in order to use the same wavelength calibration for all XGS observations, the requirement on the repeatability in those two axes is tighter.

From these simulations, we estimate the alignment tolerance that reduces R or A_{eff} by 10% (Table 1).

We performed similar calculations for the scenario with the largest gratings and find very similar numbers except that the rotation requirements on the rotation of an individual grating are a few times stricter. If subaperturing is used simply to reduce the number of gratings with the same science requirement on R, then the values in Table 1 do not change much. If subaperturing is used to achieve a larger R, then the alignment requirements will be somewhat tighter.

6.4 Effective Area and Resolving Power over the XGS Bandpass

We now present results for a grid of energies assuming perfect alignment. Figure 12 shows A_{eff} and R for different subapertur- ing. The A_{eff} given in the figure is the total effective area summed over all diffraction orders that are detected on the

Table 1 Alignment budget for baseline scenario (1σ values assuming a Gaussian distribution).

Element	Shift (mm)			Rotation (deg)		
	x	y	z	x	y	z
CAT assembly	>10	2	4	0.1	0.05	0.05
Individual grating	0.2	2	2	0.5	1	0.1
Camera assembly	0.02[a]	5	>10	1	>2	0.02[a]
individual detector	0.02	5	>10	>2	>2	0.5

[a]Both of these lead to focus errors and can be corrected in flight with the planned focusing mechanism.

detector defined in Sec. 6.1. Some chip gaps are visible in the plot of A_{eff}, but the wavelength grid is too coarse to see all of them. Since more than one order is detected for most wavelengths, the chip gaps generally lead to a reduced, but still nonzero A_{eff} at that wavelength. A Chandra-like dither pattern could be employed to reduce their impact. The shown values for R are the efficiency-weighted averages for all detected orders. When one order falls into a chip gap, the resolving power can show spikes up or down, when the order missing at that wavelength had a lower or higher than average resolving power.

6.5 Usability of the Zeroth-Order

An important question is how the presence of the gratings interferes with observations in the zeroth-order simultaneous with the dispersed spectra. The position of the zeroth-order is required for wavelength calibration of the diffracted signal, but
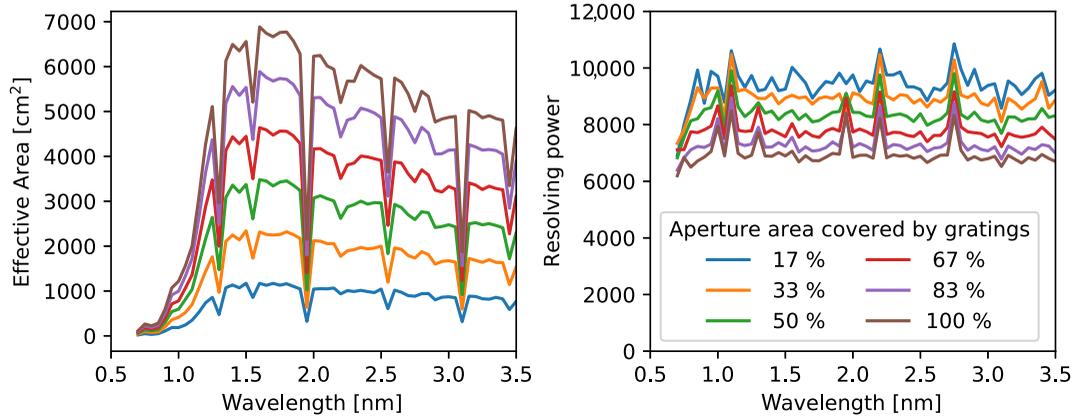
Fig. 12 A_{eff} and R for different subaperturing angles. Drops in A_{eff} occur when one of the detected orders falls into a chip gap. The R shown is averaged over all detected orders, so if one order is missing, R can show a spike upward or downward.
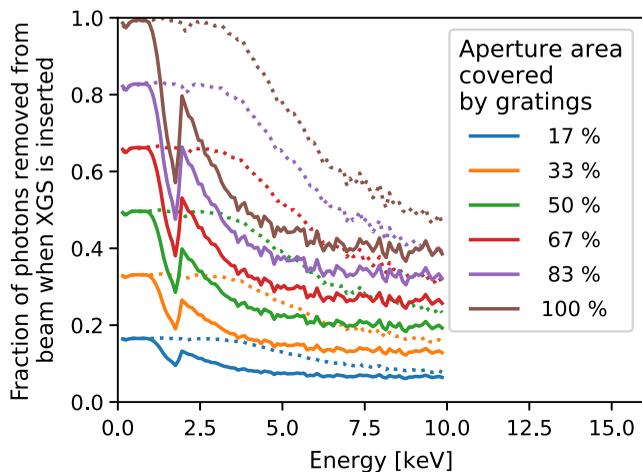

Fig. 13 Fraction of photons removed from the beam if the XGS is inserted. Solid lines are for pure Si gratings, dotted lines are for a scenario with only Pt-coated gratings. Any ratio between the two curves can be chosen, depending on the desired XGS effective area in the ~1.5 to 2 keV range. These simulations include shadowing by the gratings frames and support structure. If about two-thirds of the aperture is covered with Si gratings, the LXM or HDXI still sees about 60% to 70% of the flux above 2 keV that it would see without the XGS inserted. Even if all gratings are coated with Pt, that number is still more than 30% to 60%.

especially at energies above 2 keV, where A_{eff} of the dispersed orders is low, analysis of the zero-order microcalorimeter data becomes important. For example, in young, flaring stars it would be possible to study the mass accretion in soft x-rays in the diffracted signal and the hot Fe $K\alpha$ line in the microcalorimeter simultaneously. Figure 13 shows that the CAT gratings are mostly transparent at high energies. If two-thirds of the aperture is covered with CAT gratings, only 30% to 40% of the high-energy photons are absorbed, and these simulations already include absorption by the mounting structure of the gratings.

6.6 Calibration Tolerances

So far, no science requirement for the absolute wavelength accuracy of the XGS has been specified,[5] and thus we currently have

not studied the calibration of the instrument in detail. Table 1 gives the alignment requirements for the elements of the Lynx XGS. Once all elements are set at fixed positions, the absolute wavelength scale can be calibrated, e.g., by observations of an astronomical emission line source, such as Capella. However, the wavelength scale changes if the position of the zeroth-order changes or optical elements move. The position of the zeroth-order can be measured in the microcalorimeter, typically with a high signal-to-noise (Sec. 6.5). In order to achieve an absolute wavelength calibration accuracy of 25 km s^{-1}, the relative change of the location where the dispersed signal is detected compared to the position where it was detected during calibration is then about 10^{-4}, which corresponds to 0.05 mm. To reach this level, either the focal plane must be temperature controlled to limit thermal expansion or the relevant temperatures are measured and the change of the XGS camera position with respect to the zeroth-order is calibrated for different temperatures. Similarly, this requires that the positions of the gratings are stable. Either a calibration observation is performed each time after the XGS gratings are inserted into the beam or the insertion mechanism has to provide a highly repeatable position.

7 Future Improvements and Design Options

In the previous sections, we show that a relatively simple design fulfills the science requirements for the XGS. In this section, we want to discuss design options that could improve the capability of the instrument at the cost of a slightly more complex design. It is beyond the scope of the current work to perform a detailed trade study on each of them.

7.1 Grating Positions

An easy step to improve R is to minimize the average deviation of each grating from the Rowland torus instead of simply placing the center of each grating onto the torus as discussed in Sec. 6.2.

7.2 Detailed Grating Placement

In Figs. 5 and 8, gratings are placed to homogeneously fill the area behind the mirrors and each grating has space for a 1-mm wide mounting frame. In practice, a structure as large as the XGS grating assembly will need a few thicker and more substantial support structures which will introduce wider shadows.
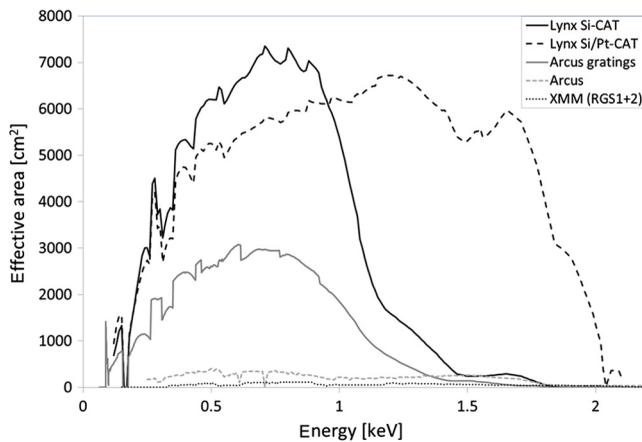
Fig. 14 Example effective area calculations for full telescope coverage (360 deg), using a silicon meta-shell mirror model for mirror effective area. "Arcus gratings" (gray line) shows Lynx performance with today's state-of-the-art 4-μm-deep CAT gratings fabricated for Arcus and Arcus-like support structures. "Lynx Si-CAT" (black line) shows expected future performance for deeper CAT gratings with narrower support structures. "Lynx Si/Pt-CAT" (dashed line) shows theoretical future performance for Pt-coated CAT gratings. Similar to the full ray-trace results, effective area of 4000 cm^2 at 0.6 keV can be achieved with $\approx$2/3 telescope coverage, whether using coated or uncoated deeper CAT gratings. Science trades can be done in the future to determine which fraction of the grating arrays should hold coated or uncoated gratings. For comparison, we also show the expected effective area for the Arcus mission (short-dashed line) and for the XMM-Newton RGS (dotted line).

On the other hand, the mirror effective area is not equally distributed over the entire area either. The mounting structures of the grating assembly should be aligned with the support structures of the mirror to reduce the area lost. A detailed study of this cannot be performed before the mirror is better specified, but our experience from the detailed Arcus design and ray-tracing in phase A[31] is that this will have negligible impact on R and will change A_{eff} by a few percent at most.

Another consideration is to limit the radius over which the gratings are placed since the photon energies best reflected off the mirrors depend on the mirror graze angle and thus the radius.

7.3 Coated Gratings

The simulations above assume uncoated Si CAT gratings. Coating the surface of these gratings with a metal, e.g., Pt,[20] would increase the grating efficiency at higher energies and thus significantly improve the effective area of the XGS at short wavelength. At the same time, those photons would be lost from the zeroth-order, reducing the effective area for high-energy photons there (see Figs. 13 and 14). It may not be beneficial to coat all gratings, since below ~1 keV the effective area is actually higher for uncoated Si gratings (see Fig. 14). However, if even a small fraction of gratings is coated, the effective area below 12Å could already be increased by a factor of a few.

7.4 Two Grating Traces

Figure 10 shows how the resolving power decreases as more and more gratings are used because some of them must be placed at less preferable subaperturing angles. This problem can be overcome by generating two spectral traces on the detector, similar to how it is done for Chandra/HETG,[32] where the gratings that

make up the high-energy grating and the medium-energy grating are mounted such that their dispersion directions differ a little. The resulting signal is an X on the detector, where each diagonal belongs to one of the respective grating sets. In the Lynx XGS, we would rotate the dispersion direction for a fraction of the gratings that are located at the best subaperturing angles (as judged from ray-tracing preflight) by 0.25 degrees and the remaining gratings by −0.25 deg. This would give us two traces on the detector array which are diverging with an average distance of 5 mm, more than enough to separate them easily, but still far away from the detector edges. Similar to Chandra/HETG, the data reduction software would extract two separate spectra and the observer could choose to analyze only the spectrum with the highest R, but limited A_{eff} for science questions that require the best spectral resolution, or fit them jointly to take advantage of the full effective area. The main drawback of this approach is that it is more likely that spectra overlap for observations of crowded fields, such as the Orion Nebula Cloud, where many targets may produce bright grating spectra, but those targets would be complicated to observe and reduce in any case.

A variant of this idea is to mount the gratings on several different sectors that can be moved into the beam independently, e.g., in sectors that are 30 deg wide. In this case, an observer might specify to insert only the gratings in the −15 deg to +15 deg sector, while another observation could be done with the gratings in the sectors −45 deg to −15 deg, −15 deg to +15 deg, and +15 deg to +45 deg. This would lower the resolving power, but deliver three times the effective area compared to the first observation.

7.5 Detectors for the XGS

Section 2.2 describes the detector currently planned and used in our ray-trace simulations. The requirements are derived from the HDXI. For the XGS, longer detectors, preferably curved (as possible for CCDs), would reduce the area lost to chip gaps. For spectroscopy of a single point source, the detector only has to be a few mm wide in cross-dispersion direction, potentially reducing mass, power, cost, and data rate compared to the detectors currently simulated.

7.6 Chirp

The use of chirped gratings promises great benefits. A smaller number of larger gratings can deliver the same effective area and resolving power, presumably at significantly reduced cost. We comment on the fabrication of chirped gratings below.

7.7 Multiobject Spectroscopy

Our design for the Lynx XGS is slitless. Thus, all x-ray sources in the field of view contribute to the dispersed signal. Two sources separated in dispersion direction are seen as a single spectrum where features (e.g., emission lines) seem to be red- or blueshifted. If two sources are offset from each other in cross-dispersion direction, two separate spectral traces can be extracted if the separation is large enough. When using larger grating membranes, the dispersed signal is wider and close sources will blend (Fig. 8); wider traces also require larger spectral extraction regions which contain more background events. The current design is not optimized for multiobject spectroscopy, but if required, the size of the facets in cross-dispersion

direction can be reduced to reduce the width of the spectral trace in cross-dispersion direction, incurring a small loss of efficiency due to the increased area covered by frames and mounting structures.

8 Future Technology Development for CAT Grating Fabrication

In order for a CATXGS to perform at the level envisioned for Lynx, both CAT grating and readout technologies have to be improved. In this article, we only discuss CAT grating technology, while development for various readout technologies is discussed in other papers in this special section.

CAT grating technology has improved since its last official TRL evaluation in 2016, and we consider it to be at TRL 5-6 for the purposes of the Arcus mission. However, if we simply populate the Lynx mirror aperture with existing CAT gratings of the Arcus design, we see in Fig. 14 that the effective area performance falls short of requirements.

There are three main effective area performance issues that need to be addressed: Arcus-like support structures block too much of the x-ray flux that exits from the mirror array, grating diffraction efficiency needs to be improved, and high-diffraction efficiency needs to extend to higher energies.

Reducing the area blocked by support structures is relatively straightforward through definition of these structures in our initial lithography steps, but there will be a mechanical limit where the grating membrane becomes too weak to survive fabrication (with sufficient yield) or launch loads. Our current goal for Lynx is to increase the open area fraction for both the L1 and L2 support meshes to 90% from 82% and 81%, respectively. Larger-scale structures, such as the grating frames and a grating array structure (GAS) that holds the grating facets in place, need to be made as narrow as possible in the plane perpendicular to the x-ray propagation direction. They also need to take maximum advantage of the nontransmitting areas of the mirror array by putting as much of these structures in the x-ray shadow from mirror support structures. For example, for a strawman meta-shell mirror array design consisting of 12 concentric, ~1 cm-thick structural cylinders, we could place two rows of 5-cm-wide gratings to bridge the ~0.1 m gap between cylinders, and design most of the GAS to lie in the shadow of the cylinders.

The diffraction efficiency of CAT gratings can be significantly improved by going to smaller blaze angles and simultaneously increasing grating depth d (see Fig. 2). Throughout this article, we assumed an average incidence angle of $\alpha = 1.6$ deg, grating depth of $d = 5.73$ μm, and a grating bar width $b = 40$ nm for 200-nm-period gratings. Compared to current gratings, this increases diffraction efficiency by decreasing α and increasing d and places the readout array closer to the focus. Compared to Arcus ($\alpha = 1.8$ deg, $d = 4$ μm, and $b = 60$ nm), we therefore need to develop etch recipes for deeper etches and thinner grating bars. We have achieved such depths and widths separately in our past explorations. However, development of an integrated process on the scale of Lynx gratings is a major effort that remains to be done.

The critical angle in vacuum is a function of x-ray wavelength λ and the atomic number Z of the material at the vacuum/solid interface: $\theta_c(\lambda, Z) \propto \lambda\sqrt{Z}$. With $\alpha = 1.6$ deg and gratings made from silicon we find that $\theta_c(\lambda, 14) = \alpha$ around $\lambda = 1.15$ nm or $E = 1.05$ keV. To avoid the drop-off in effective area above this energy seen for Si gratings in Fig. 14, we can use the same methods that are used to extend the energy range of

x-ray mirrors: coating of substrates with thin films of high-Z materials. We have previously used atomic layer deposition of platinum onto silicon CAT gratings and achieved the expected increase in the critical angle.[20] However, detailed studies of the diffraction efficiency of such coated CAT gratings have yet to be conducted. The curve labeled "Lynx Si/Pt-CAT" in Fig. 14 is a theoretical prediction based on ideal Si CAT gratings with $b = 28$ nm and a 6-nm-thick film of Pt on both sides of the Si grating bars. This is a challenging and so far unproven geometry. Currently there is no well-defined effective area requirement above ~1 keV, except that the useful band for the XGS should extend to 2 keV. It is therefore unknown whether metal-coated CAT grating technology has to be advanced to the level shown in Fig. 14, or whether smaller effective area between 1 and 2 keV is sufficient.

Our simulations show that adding a chirp to the grating period has great appeal and potential to significantly increase resolving power. We are currently developing patterning methods for 200-nm-period CAT gratings using 4× projection lithography using e-beam written masks as is standard in the semiconductor industry. This method in principle should allow the generation of chirped grating patterns in straightforward fashion.

The "ideal" CATXGS would consist of a small number (a few hundred) of gratings that conform to the Rowland torus everywhere and feature the same blaze angle throughout the converging beam of the telescope. This would require bent gratings and the ability to tailor the grating bar angle across each grating. For the large radii of curvature of the Rowland torus, bending of the thin transmission gratings is not out of the question, and simple bending experiments have been promising.[33] However, producing the ultrahigh aspect-ratio nanometer-scale features with smooth grating bar sidewalls required for CAT gratings, while at the same time varying the bar angle as a function of position on the grating is challenging.

The future technology development described above to get from today's state-of-the-art to the required Lynx performance does not contain new groundbreaking discoveries or inventions. Rather, it requires persistent and systematic gradual improvement of fabrication, alignment, and testing methods, and refinement of mechanical and optical models. With proper funding, we are confident that TRL 5 and 6 can be achieved within a schedule compatible with Lynx, should it be selected as NASA's next large astrophysics mission.

9 Summary and Discussion

We present a design and ray-traces for an XGS on Lynx using CAT gratings. CAT gratings covering about two-thirds of the total telescope aperture can disperse a spectrum onto a strip of detectors and achieve $R > 5000$ and $A_{\text{eff}} > 4000$ cm^2 at an energy of 0.6 keV and can thus meet the Lynx science requirements for a grating spectrometer. In our baseline case of flat 50 mm × 20 mm gratings about 4000 gratings would be required, but we also show that larger gratings deliver acceptable R for certain subaperture regions. The use of larger gratings avoids photon loss due to mounting structures and reduces cost. Combining the advantages of both approaches, we suggest to use larger gratings where they are close to tangential to the Rowland torus and smaller gratings where deviations are larger. This combination allows us to cover the required area of the aperture with only about 2000 gratings. In this design, we expect $R \approx 7500$ based on our current simulations. We described two

ways to increase R significantly. First, our baseline case makes the most conservative assumptions for the scattering properties of the mirror. A mirror with significant difference in the in-plane and out-of-plane scatter would automatically lead to better R for the same subaperturing. Second, a correction of the grating position to minimize the average deviation from the Rowland torus can increase R over the numbers given here without additional grating or mirror development effort.

To realize $R > 5000$ and $A_{eff} > 4000$ cm^2 with gratings up to 50 mm $\times$ 50 mm requires some development effort for CAT grating production, but no fundamentally new technology. In particular, the grating size, the depth of the etch, and the parameters of the L1 and L2 support structures need to be improved. Chirped gratings overcome the size limitations and thus deliver a high R almost independent of the grating size. In this study, we chose the chirp separately for each grating; future ray-trace work will determine how many different types of gratings are required depending on the value of R. In either case, only about 300 gratings of 80 mm $\times$ 160 mm can deliver $A_{eff} > 4000$ cm^2. However, the fabrication and performance of large chirped gratings remains to be demonstrated.

For pure Si gratings about 40% of the hard x-rays still reach the focal point; even if some fraction of the gratings will be coated with Pt, hard energies can still be studied with the microcalorimeter.

We also present ray-tracing calculations to estimate the alignment tolerances for our CAT XGS design. In many degrees of freedom, requirements are so loose that simple machining tolerances are sufficient.

In summary, we present a design for a CAT grating-based spectrograph that can be realized with steady development in CAT grating technology. Our design covers about two-thirds of the aperture to achieve $R > 5000$ and $A_{eff} > 4000$ cm^2, but still allows most high-energy photons to pass through to the detectors at the focal plane. There are several options in terms of grating size and subaperturing, but even with the most basic design, Lynx requirements can be met with ample margin.

Acknowledgments

References

1. J. A. Gaskin et al., "Lynx mission concept status," *Proc. SPIE* **10397**, 103970S (2017).
2. J. A. Gaskin et al., "The Lynx x-ray observatory: an overview," *J. Astron. Telesc. Instrum. Syst.* **5**(2) (2019).
3. M. J. Collon et al., "Silicon pore optics development for ATHENA," *Proc. SPIE* **9603**, 96030K (2015).
4. M. J. Collon et al., "Making the ATHENA optics using silicon pore optics," *Proc. SPIE* **9144**, 91442G (2014).
5. F. Özel and A. Vikhlinin on behalf of the Lynx team, "The Lynx mission concept study interim report," arXiv:1809.09642 (2018).
6. R. K. Heilmann et al., "Diffraction efficiency of 200-nm-period critical-angle transmission gratings in the soft x-ray and extreme ultraviolet wavelength bands," *Appl. Opt.* **50**, 1364–1373 (2011).
7. R. K. Heilmann, A. R. Bruccoleri, and M. L. Schattenburg, "High-efficiency blazed transmission gratings for high-resolution soft x-ray spectroscopy," *Proc. SPIE* **9603**, 960314 (2015).
8. R. L. McEntaffer, "Reflection grating concept for the Lynx x-ray grating spectrograph," *J. Astron. Telesc. Instrum. Syst.* **5**(2), 021002 (2019).
9. R. K. Smith et al., "Arcus: exploring the formation and evolution of clusters, galaxies, and stars," *Proc. SPIE* **10397**, 103970Q (2017).
10. W. W. Zhang et al., "Silicon meta-shell optics for Lynx," *J. Astron. Telesc. Instrum. Syst.* **5**(2) (2019).
11. M. Ahn, R. K. Heilmann, and M. L. Schattenburg, "Fabrication of ultra-high aspect ratio freestanding gratings on silicon-on-insulator wafers," *J. Vac. Sci. Technol. B* **25**(6), 2593 (2007).
12. K. Flanagan et al., "Spectrometer concept and design for x-ray astronomy using a blazed transmission grating," *Proc. SPIE* **6688**, 66880Y (2007).
13. M. Ahn, R. K. Heilmann, and M. L. Schattenburg, "Fabrication of 200 nm period blazed transmission gratings on silicon-on-insulator wafers," *J. Vac. Sci. Technol. B* **26**, 2179–2182 (2008).
14. P. Mukherjee et al., "Plasma etch fabrication of 60:1 aspect ratio silicon nanogratings with 200 nm pitch," *J. Vac. Sci. Technol. B* **28**, C6P70–C6P75 (2010).
15. A. Bruccoleri et al., "Fabrication of nanoscale, high throughput, high aspect ratio freestanding gratings," *J. Vac. Sci. Technol. B* **30**, 06FF03 (2012).
16. A. R. Bruccoleri et al., "Nanofabrication advances for high efficiency critical-angle transmission gratings," *Proc. SPIE* **8861**, 886119 (2013).
17. A. Bruccoleri et al., "Potassium hydroxide polishing of nanoscale deep reactive-ion etched ultrahigh aspect ratio gratings," *J. Vac. Sci. Technol. B* **31**, 06FF02 (2013).
18. A. R. Bruccoleri, R. K. Heilmann, and M. L. Schattenburg, "Fabrication process for 200 nm-pitch polished freestanding ultrahigh aspect ratio gratings," *J. Vac. Sci. Technol. B* **34**, 6KD02 (2016).
19. R. K. Heilmann et al., "Blazed transmission grating technology development for the Arcus x-ray spectrometer explorer," *Proc. SPIE* **10699**, 106996D (2018).
20. R. K. Heilmann et al., "Critical-angle x-ray transmission grating spectrometer with extended bandpass and resolving power >10,000," *Proc. SPIE* **9905**, 99051X (2016).
21. R. K. Heilmann et al., "Demonstration of resolving power $\lambda/\Delta\lambda >$ 10,000 for a space-based x-ray transmission grating spectrometer," *Appl. Opt.* **58**, 1223–1238 (2019).
22. R. K. Heilmann et al., "Critical-angle transmission grating technology development for high resolving power soft x-ray spectrometers on Arcus and Lynx," *Proc. SPIE* **10399**, 1039914 (2017).
23. J. Song et al., "Scanning laser reflection tool for alignment and period measurement of critical-angle transmission gratings," *Proc. SPIE* **10399**, 1039915 (2017).
24. K. P. Beuermann, H. Bräuninger, and J. Trümper, "Aberrations of a facet-type transmission grating for cosmic x-ray and XUV spectroscopy," *Appl. Opt.* **17**, 2304–2309 (1978).
25. R. K. Heilmann et al., "Critical-angle transmission grating spectrometer for high-resolution soft x-ray spectroscopy on the international x-ray observatory," *Proc. SPIE* **7732**, 77321J (2010).
26. H. M. Günther et al., "Performance of a double tilted-Rowland-spectrometer on Arcus," *Proc. SPIE* **10397**, 103970P (2017).
27. H. M. Günther, J. Frost, and A. Theriault-Shay, "Chandra-Marx/marxs: v1.1," *Zenodo* (2017).
28. H. M. Günther, J. Frost, and A. Theriault-Shay, "MARXS: a modular software to ray-trace x-ray instrumentation," *Astron. J.* **154**, 243 (2017).
29. B. D. Chalifoux et al., "Simulations of film stress effects on mirror segments for the Lynx x-ray observatory concept," *J. Astron. Telesc. Instrum. Syst.* **5**(2), 021004 (2019).
30. L. Raimondi and D. Spiga, "Mirrors for x-ray telescopes: Fresnel diffraction-based computation of point spread functions from metrology," *Astron. Astrophys.* **573**, A22 (2015).
31. H. M. Günther et al., "Ray-tracing Arcus in phase A," *Proc. SPIE* **10699**, 106996F (2018).
32. C. R. Canizares et al., "The Chandra high-energy transmission grating: design, fabrication, ground calibration, and 5 years in flight," *Publ. Astron. Soc. Pac.* **117**, 1144–1171 (2005).

33. S. N. T. Heine et al., "Laboratory progress in soft x-ray polarimetry," *Proc. SPIE* **10399**, 1039916 (2017).
34. H. M. Günther and R. K. Heilmann, "An x-ray transmission grating spectrometer for Lynx," *Proc. SPIE* **10699**, 1069914 (2018).
35. Astropy Collaboration et al., "Astropy: a community Python package for astronomy," *Astron. Astrophys.* **558**, A33 (2013).
36. Astropy Collaboration et al., "The astropy project: building an open-science project and status of the v2.0 core package," *Astron. J.* **156**, 123 (2018).
37. S. van der Walt, S. C. Colbert, and G. Varoquaux, "The NumPy array: a structure for efficient numerical computation," *Comput. Sci. Eng.* **13**(2), 22–30 (2011).
38. F. Pérez and B. E. Granger, "IPython: a system for interactive scientific computing," *Comput. Sci. Eng.* **9**, 21–29 (2007).
39. P. Ramachandran and G. Varoquaux, "Mayavi: 3D visualization of scientific data," *Comput. Sci. Eng.* **13**(2), 40–51 (2011).
40. J. D. Hunter, "Matplotlib: a 2D graphics environment," *Comput. Sci. Eng.* **9**(3), 90–95 (2007).

Hans Moritz Günther is a research scientist at MIT. He received his undergraduate and PhD degrees in physics from the University of Hamburg, Germany, in 2005 and 2009, respectively. After that, he worked at the Harvard-Smithsonian Center for Astrophysics and came to MIT in 2015. He is currently the lead developer of MARX, the ray-tracing software used for the Chandra X-ray Observatory. His science interests are in star formation using data from the radio to x-rays.

Ralf K. Heilmann is a principal research scientist at the MIT Kavli Institute for Astrophysics and Space Research, and the associate director of the Space Nanotechnology Laboratory (SNL). He received his diploma in physics from the FAU Erlangen/Nürnberg in 1991 and his MS and PhD degrees in physics from Carnegie Mellon University in 1993 and 1996, respectively. After a postdoc at Harvard, he joined the SNL and has since focused on advanced lithography and the development of x-ray optics for astronomy.